IEEE Access
Multidisciplinary | Rapid Review | Open Access Journal

Received 1 May 2023, accepted 27 May 2023, date of publication 30 May 2023, date of current version 7 June 2023.
Digital Object Identifier 10.1109/ACCESS.2023.3281459

RESEARCH ARTICLE

Study on Single-Loop FCS-MPC for DC-Based DFIG System

SHAOMIN YAN, XIAOJIE GAO, YONGHAO LU, YUE CUI, AND YUHAN CAI
School of Engineering, Qufu Normal University, Rizhao 276800, China
Corresponding author: Shaomin Yan (qfnuyan@163.com)

This work was supported in part by the Shandong Provincial Natural Science Foundation under Grant ZR2019MEE053, and in part by the Shandong Provincial Graduate Education Quality Improvement Project under Grant SDYAL17075.

ABSTRACT Doubly fed induction generator (DFIG) system suffers from complex control structure, slow dynamic response speed and cumbersome parameter design due to its traditional cascaded dual-loop control strategy. A single-loop finite control set model predictive control (SLMPC) is proposed in the paper for DC-based DFIG in DC grid, which simplifies its control structure and parameter design, and enhances system dynamic response. There are three improved aspects. First, the single-loop control structure is proposed to eliminate intermediate link in dual-loop cascaded structure, and enhance system dynamic response. Second, system reduced-order discretization algorithm is proposed by differential and integral discretization method to reduce finite control set model predictive control strategy (FCS-MPC) design difficulty. Third, cost function with nonlinear additional current limiting function is designed to protect system from overcurrent effectively. Finally, the feasibility of proposed strategy is verified by simulations and experiments.

INDEX TERMS DFIG, FCS-MPC, current limiting function, single-loop control strategy, differential and integral discretization.

I. INTRODUCTION

wind power now represents a vital and growing renewable energy sources [1], and the installation capacity of doubly fed induction generator (DFIG) has been increasing rapidly so far. And DFIG is widely used not only in AC-based wind-farms with its merits of high-power density and efficiency [2], but also in DC-based windfarms with fast development of high voltage direct current (HVDC) [3], [4]. Compared with the traditional DFIG, DC-based DFIG has the advantages of simple structure and low cost [5], [6]. This paper mainly studies on control strategy of double-controlled DC-based DFIG.

Dual-loop cascaded control structure is generally applied for DC-based DFIG to improve system performance [7], [8], [9], [10], [11], [12]. In [13], a direct resonant control scheme is presented to suppress the current harmonics and reduce the torque ripple simultaneously. In [14], a distributed active and reactive power coordination scheme is proposed to improve the utilization of converter capacity and efficiency. In [15], a control strategy based on multiple reference frame is designed to decrease torque ripple. In [16], an active damping control strategy is proposed with adjustment of dual-loop PI controllers to damp high-frequency resonance. In [17], a coordinated power control structure is proposed to reduce converter loss and enhance system operation reliability. In [18], a coordinated repetitive control strategy is proposed to ease pulsations of reactive power and electromagnetic torque, and improve the current quality. However, cascaded dual-loop control structure has some shortcomings such as control structure complexity and control parameters design difficulty, which affects system performance. Besides, PI controller has good control ability in an only small range of wind speed, with the drawbacks of limitations about the steady-state magnitude and phase errors, and slow response speed [19], [20].

Finite control set model predictive control strategy (FCS-MPC) is an excellent control strategy with the merits of strong anti-coupling performance and fast response speed [21], which is applied in various electric machine

The associate editor coordinating the review of this manuscript and approving it for publication was Derek Abbott.

control [22], [23], [24], [25], [26] and other power electronics field [27], [28], [29], [30]. In [31], a predictive torque control is presented to promote the estimation accuracy of flux linkage and rotor speed in the feedback-correction-based dual reference frame. In [32], a multiple-vector-based model predictive power control is presented to restrain current distortion and high-power ripples. In [33], a predictive control scheme Laguerre function-based is proposed to shorten computation burden and improve control precision. In [34], an improved predictive direct power control algorithm is designed in a switching period to reduce current THD and electromagnetic torque ripple. In [35], a direct power control under normal and voltage sag operation is proposed to avoid high peak currents of stator and rotor, and improve system safety. In [36], a low complexity robust control strategy is proposed to compensate unbalanced stator current and harmonic, and improve system power quality. In [37], a time efficient FCS-MPC scheme is proposed to obtain longer prediction horizons and better control performance. However, cascaded dual-loop proportional-integral and model predictive control (PI-MPC) control structure is adopted in the most mentioned literatures, which increases design complexity and restricts system response speed.

In order to solve above problems, the single-loop FCS-MPC control strategy (SLMPC) is proposed in the paper, and the key contributions are summarized as follows.

1) A SLMPC strategy is proposed to eliminate the intermediate link of traditional cascaded dual-loop structure, and improve system performance.

2) System state equation is derived, and system reduced-order discretization algorithm is proposed to simplify second-order predictive equation.

3) Current limiting function is designed to limit excessive current and protect system. Finally, simulations and experiments are designed to show feasibility and efficiency of designed strategy.

And rest of the paper is organized as follows. The DC-based DFIG system model is built in Section II. The proposed SLMPC and traditional PI-MPC strategies are designed in Section III. The system simulations are in Section IV. The system experiments are in Section V. The conclusions are illustrated in Section VI.

II. DC-BASED DFIG SYSTEM MODEL

Double-controlled DC-based DFIG system includes wind turbine, DFIG, gearbox, stator side converter (SSC) and rotor side converter (RSC), which is depicted in Fig. 1. RSC and SSC are linked to the DC bus.

DFIG system model is expressed as [8]

$$\begin{cases} u_{sd} = \frac{d\psi_{sd}}{dt} + R_s i_{sd} - \omega_1 \psi_{sq} \\ u_{sq} = \frac{d\psi_{sq}}{dt} + R_s i_{sq} + \omega_1 \psi_{sd} \\ u_{rd} = \frac{d\psi_{rd}}{dt} + R_r i_{rd} - \omega_s \psi_{rq} \\ u_{rd} = \frac{d\psi_{rq}}{dt} + R_r i_{rq} + \omega_s \psi_{rd} \end{cases} \tag{1}$$

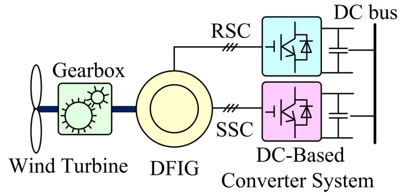

FIGURE 1. DC-based double-controlled DFIG system.

$$\begin{cases} \psi_{sd} = L_m i_{rd} + L_s i_{sd} \\ \psi_{sq} = L_m i_{rq} + L_s i_{sq} \\ \psi_{rd} = L_m i_{sd} + L_r i_{rd} \\ \psi_{rq} = L_m i_{sq} + L_r i_{rq} \end{cases} \tag{2}$$

$$\begin{cases} T_m - T_e = J\frac{d\omega_m}{dt} = \frac{J}{n_p}\frac{d\omega_r}{dt} \\ T_e = \frac{3}{2}\frac{L_m n_p}{L_s}(\psi_{sd} i_{rq} - \psi_{sq} i_{rd}) \end{cases} \tag{3}$$

where u, ψ, and i are voltage, flux and current, respectively. The subscripts (rd, rq, sd, and sq) are rotor's and stator's dq components respectively; ω_1 and ω_s are synchronous and slip angular velocity. L_s, L_m and L_r are stator, mutual and rotor inductance respectively. T_e and T_m are electromagnetic and mechanical torque. Besides, R_r and R_s are rotor resistance and stator resistance. J is generator rotational inertia.

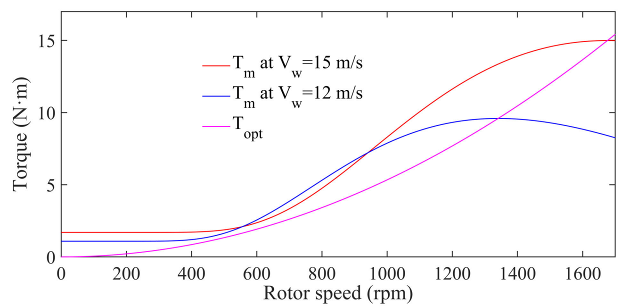

FIGURE 2. Wind turbine torque curves.

Wind turbine and gearbox system models are considered as a whole model, and torque curves (T_m) at wind speed of 12 and 15 m/s are shown in Fig. 2.

And the optimal torque (T_{opt}) is expressed as

$$\begin{cases} T_{opt} &= k_1 {V_w}^2 + k_2 V_w + k_3 \\ n_{ropt} &= \dfrac{60\omega_{ropt}}{2\pi n_p} = k_4 V_w \end{cases} \tag{4}$$

where V_w, n_{ropt} and ω_{ropt} are wind speed, optimal rotor speed and rotor angular frequency; n_p is polar logarithm; k_1-k_4 are the max power curve coefficients and set to 0.0667, 3.14×10^{-6}, 7.0×10^{-6} and 111.8, respectively [8].

III. SINGLE-LOOP FCS-MPC CONTROL STRATEGY

SLMPC strategy is presented to enhance system dynamic performance and decrease system design complexity. First, second-order system equations are derived. Second, a system reduced-order discretization method is applied to simplify order of DFIG system model. Finally, the single-loop FCS-MPC scheme is designed based on discretization method.

A. MODEL PREDICTIVE EQUATION ESTABLISHING

1) SECOND-ORDER SYSTEM MODEL

Substituting (2) in (1), DFIG model based on stator flux-orientation is expressed as

$$\begin{cases} \dfrac{d\psi_{sd}}{dt} = \beta R_s i_{rd} - \dfrac{R_s}{L_s}\psi_{sd} + u_{sd} + \omega_1\psi_{sq} \\ \dfrac{d\psi_{sq}}{dt} = \beta R_s i_{rq} - \dfrac{R_s}{L_s}\psi_{sq} + u_{sq} - \omega_1\psi_{sd} \\ \dfrac{di_{rd}}{dt} = \dfrac{1}{\alpha}[\alpha\omega_s i_{rq} - \lambda_s i_{rd} - \beta a] + \dfrac{1}{\alpha}u_{rd} \\ \dfrac{di_{rq}}{dt} = -\dfrac{1}{\alpha}[\alpha\omega_s i_{rd} + \lambda_s i_{rq} + \beta b] + \dfrac{1}{\alpha}u_{rq} \end{cases} \tag{5}$$

where $\alpha = (L_s L_r - L_m{}^2)/L_s\text{m}/L_s$, $\lambda = R_r + \beta^2 R_s$, $a = (u_{sd} + \omega_r\psi_{sq} - R_s\psi_{sd}/L_s)$, $b = (u_{sq} - \omega_r\psi_{sd} - R_s\psi_{sq}/L_s)$.

Taking the derivative of (3), (6) is given as

$$\frac{d^2\omega_r}{dt^2} = \frac{n_p}{J}[\frac{dT_m}{dt} - \frac{dT_e}{dt}] \tag{6}$$

besides, dT_e/dt is expressed as

$$\begin{aligned} \frac{dT_e}{dt} &= \frac{3}{2}\frac{L_m n_p}{L_s}(\frac{d\psi_{sd}}{dt}i_{rq} + \frac{di_{rq}}{dt}\psi_{sd} - \frac{d\psi_{sq}}{dt}i_{rd} - \frac{di_{rd}}{dt}\psi_{sq}) \\ &= \frac{3}{2}\frac{L_m n_p}{L_s}\begin{bmatrix} (u_{sd} - \frac{R_s}{L_s}\psi_{sd} + \omega_1\psi_{sq} + \beta R_s i_{rd})i_{rq} \\ -\frac{\psi_{sd}}{\alpha}(\lambda_s i_{rq} - \alpha\omega_s i_{rd} - \beta b) \\ -(u_{sq} - \frac{R_s}{L_s}\psi_{sq} - \omega_1\psi_{sd} + \beta R_s i_{rq})i_{rd} \\ +\frac{\psi_{sq}}{\alpha}(\lambda_s i_{rd} + \alpha\omega_s i_{rq} - \beta a) \end{bmatrix} \\ &\quad + \frac{3}{2}\frac{L_m n_p}{L_s}(\frac{\psi_{sd}}{\alpha}u_{rq} - \frac{\psi_{sq}}{\alpha}u_{rd}) \end{aligned} \tag{7}$$

Thus, $d^2\omega_r/dt^2$ is expressed as

$$\frac{d^2\omega_r}{dt^2} = \frac{n_p}{J}[\frac{dT_m}{dt} - (f_x + u_{eq})] \tag{8}$$

where

$$f_x = \frac{3}{2}\frac{L_m n_p}{L_s}\begin{Bmatrix} (\beta R_s i_{rd} - \frac{R_s}{L_s}\psi_{sd} + \omega_1\psi_{sq} + u_{sd})i_{rq} \\ -\frac{\psi_{sd}}{\alpha}[-\frac{1}{\alpha}(\lambda_s i_{rq} + \alpha\omega_s i_{rd} + \beta b) + \frac{1}{\alpha}u_{rq}] \\ -(\beta R_s i_{rq} - \frac{R_s}{L_s}\psi_{sq} - \omega_1\psi_{sd} + u_{sq})i_{rd} \\ +\frac{\psi_{sq}}{\alpha}[\frac{1}{\alpha}(\alpha\omega_s i_{rq} - \lambda_s i_{rd} - \beta a) + \frac{1}{\alpha}u_{rd}] \end{Bmatrix},$$

$$u_{eq} = \frac{3}{2}\frac{L_m n_p}{L_s}[\frac{\psi_{sd}}{\alpha}u_{rq} - \frac{\psi_{sq}}{\alpha}u_{rd}].$$

So, system equations from (5) and (8) are summarized as

$$\begin{cases} \dfrac{d\psi_{sd}}{dt} = \beta R_s i_{rd} - \dfrac{R_s}{L_s}\psi_{sd} + u_{sd} + \omega_1\psi_{sq} \\ \dfrac{d\psi_{sq}}{dt} = \beta R_s i_{rq} - \dfrac{R_s}{L_s}\psi_{sq} + u_{sq} - \omega_1\psi_{sd} \\ \dfrac{di_{rd}}{dt} = \dfrac{1}{\alpha}[\alpha\omega_s i_{rq} - \lambda_s i_{rd} - \beta a] + \dfrac{1}{\alpha}u_{rd} \\ \dfrac{d^2\omega_r}{dt^2} = \dfrac{n_p}{J}[\dfrac{dT_m}{dt} - (f_x + u_{eq})] \end{cases} \tag{9}$$

State variables (ω_r, i_{rd}, ψ_{sd}, ψ_{sq}) could be controlled directly by $u_{sd,q}$, $u_{rd,q}$ in single loop control structure, which reduces system parameters design complexity and improves system response.

dT_m/dt could not be obtained directly, and second-order system discretization is not accurate enough with conventional Euler formula for FCS-MPC. Consequently, a system reduced-order discretisation algorithm is proposed to solve the mentioned problems.

2) SYSTEM REDUCED-ORDER DISCRETIZATION ALGORITHM

In order to reduce design difficulty of FCS-MPC for second-order system, a reduced-order algorithm based on differential and integral discretization algorithm is used to simplify second-order to first-order system.

Integrating (8), the second-order equation is converted as

$$\frac{d\omega_r}{dt} = \frac{n_p}{J}[T_m - \int(f_x + u_{eq})dt] \tag{10}$$

Differential and integral discretization method based on Euler formula is gained as

$$\begin{cases} \dfrac{dx}{dt} = \dfrac{x(k+1) - x(k)}{T} \\ \displaystyle\int xdt = \sum_{i=1}^{k} x_i T \end{cases} \tag{11}$$

where x, x_i and T are state variables and sampling time.

So, $d\omega_r/dt$ and $\int(f_x + u_{eq})/dt$ in (11) are shown as

$$\begin{cases} \dfrac{d\omega_r}{dt} = \dfrac{\omega_r(k+1) - \omega_r(k)}{T} \\ \displaystyle\int(f_x + u_{eq})dt = \sum_{i=1}^{k}(f_x + u_{eq})T = \sum_{i=1}^{k} f_x T \\ \displaystyle + \sum_{i=1}^{k-1} u_{eq}(k-1)T + u_{eq}(k)T \end{cases} \tag{12}$$

From (10) and (12), $\omega_r(k+1)$ is gained as

$$\begin{aligned} \omega_r(k+1) &= \frac{n_p T}{J}[T_m(k) - \sum_{i=1}^{k} f_x(k)T \\ &\quad - \sum_{i=1}^{k-1} u_{eq}(k-1)T] + \omega_r(k) + \frac{n_p T^2}{J}u_{eq}(k) \end{aligned} \tag{13}$$

Similarly, system equations are discretized as

$$\begin{cases} \omega_r(k+1)=\dfrac{n_pT}{J}\left[\begin{array}{c}T_m(k)-\sum\limits_{i=1}^{k}f_x(k)T\\ -\sum\limits_{i=1}^{k-1}u_{eq}(k-1)T\end{array}\right]\\ +\omega_r(k)+\dfrac{n_pT^2}{J}u_{eq}(k)\\ i_{rd}(k+1)=\dfrac{\alpha-\lambda_sT}{\alpha}i_{rd}(k)+\omega_sTi_{rq}(k)\\ -\dfrac{\beta T}{\alpha}a+\dfrac{T}{\alpha}u_{rd}(k)\\ \psi_{sd}(k+1)=(1-\dfrac{R_sT}{L_r})\psi_{sd}(k)+\omega_1T\psi_{sq}(k)\\ +\beta_sR_sTi_{rd}(k)+Tu_{sd}(k)\\ \psi_{sq}(k+1)=(1-\dfrac{R_sT}{L_r})\psi_{sq}(k)+\omega_1T\psi_{sd}(k)\\ +\beta_sR_sTi_{rq}(k)+Tu_{sq}(k)\end{cases} \tag{14}$$

where $\omega_r(k+1)$, $i_{rd}(k+1)$, $\psi_{sd}(k+1)$ and $\psi_{sq}(k+1)$ are values of rotor current and stator flux at $(k+1)$th.

According to MPC theory, predictive values (ω_r^p, i_{rd}^p, ψ_{sd}^p and ψ_{sq}^p) are given as

$$\begin{cases} \omega_r^p=\omega_r(k+1)\\ i_{rd}^p=i_{rd}(k+1)\\ \psi_{sd}^p=\psi_{sd}(k+1)\\ \psi_{sq}^p=\psi_{sq}(k+1)\end{cases} \tag{15}$$

B. COST FUNCTIONS OF RSC AND SSC

Cost functions are designed as (16) to track targets of rotor angular frequency, current and stator flux. Current limiting function is designed as (17) and eliminates all switch states that cause overcurrent.

$$\begin{cases} g_{RSC}=k_{r1}|i_{rd}^*-i_{rd}^p|+k_{r2}|\omega_r^*-\omega_r^p|+f_{lim}(i_{rd,q}^p)\\ g_{SSC}=k_{s1}|\psi_{sd}^*-\psi_{sd}^p|+k_{s2}|\psi_{sq}^*-\psi_{sq}^p|+f_{lim}(i_{sd,q}^p)\end{cases} \tag{16}$$

$$\begin{cases} f_{lim}(i_{rd,q}^p)=\begin{cases}\infty & |i_{rd,q}^p|>i_{rd,qmax}\\ 0 & |i_{rd,q}^p|\le i_{rd,qmax}\end{cases}\\ f_{lim}(i_{sd,q}^p)=\begin{cases}\infty & |i_{sd,q}^p|>i_{sd,qmax}\\ 0 & |i_{sd,q}^p|\le i_{sd,qmax}\end{cases}\end{cases} \tag{17}$$

where $f_{lim}(i_{rd,q}^p)$ and $f_{lim}(isd,q^p)$ are current limiting functions; $i_{rd,qmax}$ and $i_{sd,qmax}$ are allowable maximum currents; k_{r1}, k_{r2}, k_{s1} and k_{s2} are weight coefficients. All targets are denoted by the superscript '*' in the paper.

Predictive currents in current limiting function are obtained by Euler differential discretization method from (1), (2), (5) and (11).

$$\begin{cases} i_{rd}^p=i_{rd}(k+1)=\dfrac{\alpha-\lambda_sT}{\alpha}i_{rd}(k)+\omega_sTi_{rq}(k)\\ +\dfrac{Tu_{rd}(k)-\beta Ta}{\alpha}\\ i_{rq}^p=i_{rq}(k+1)=\dfrac{\alpha-\lambda_sT}{\alpha}i_{rq}(k)+\omega_sTi_{rd}(k)\\ +\dfrac{Tu_{rq}(k)-\beta Tb}{\alpha}\\ i_{sd}^p=i_{sd}(k+1)=i_{sd}(k)\\ +\dfrac{T}{L_s}\left[\begin{array}{c}\frac{L_m}{\alpha}\left[\begin{array}{c}\lambda_si_{rd}(k)-\alpha\omega_si_{rq}(k)\\ -\beta a-u_{rd}(k)\end{array}\right]\\ +\omega_1\psi_{sq}(k)-\frac{R_s}{L_s}\psi_{sd}(k)\\ +\frac{R_sL_m}{L_s}i_{rd}(k)+u_{sd}\end{array}\right]\\ i_{sq}^p=i_{sq}(k+1)=i_{sq}(k)\\ +\dfrac{T}{L_s}\left[\begin{array}{c}\frac{L_m}{\alpha}\left[\begin{array}{c}\lambda_si_{rq}(k)+\alpha\omega_si_{rd}(k)\\ +\beta b-u_{rq}(k)\end{array}\right]\\ -\omega_1\psi_{sd}(k)-\frac{R_s}{L_s}\psi_{sq}(k)\\ +\frac{R_sL_m}{L_s}i_{rq}(k)+u_{sq}\end{array}\right]\end{cases} \tag{18}$$

Tracking targets in (16) are calculated as follows.

If electromagnetic transient and stator resistance voltage are ignored and stator flux vector direction coincides with d-axis, stator flux targets are given from (5) as

$$\begin{cases} \psi_{sd}^* &=\dfrac{V_s^*}{\omega_1^*}\\ \psi_{sq}^* &=0\end{cases} \tag{19}$$

where $V_s^*$is rated stator voltage.

If stator reactive current is kept at 0, rotor active current target (i_{rd}^*) is given from (2) as

$$i_{rd}^*=\frac{\psi_{sd}^*}{L_m} \tag{20}$$

When DFIG operates at MPPT mode, rotor speed target (ω_r^*) is given from (4) as

$$\omega_r^*=\omega_{ropt}=\frac{2\pi n_p(k_4V_w)}{60} \tag{21}$$

C. VOLTAGE VECTOR SEEKING ALGORITHM

To minimize current errors in g_{SSC} and g_{RSC}, optimal voltage vector equation is expressed in (22).

$$\begin{cases} u_{opt} &=u_\gamma\\ \gamma &=\text{arg}\min g[f_{(\omega,i,\psi)}(u_x)]\ x\in[0,1,\ldots,7]\end{cases} \tag{22}$$

where γ represents voltage vector subscript of minimum designed cost function.

Connection between switch status and voltage vector is expressed as (23) and summarized in Table 1.

$$u=\frac{2}{3}U_{dc}(S_a+S_be^{j\frac{2}{3}\pi}+S_ce^{-j\frac{2}{3}\pi})e^{-j\theta} \tag{23}$$

where S_a, S_b, and S_c represent IGBTs' switch status of phase a, b and c respectively. $e^{-j\theta}$ is rotation factor. U_{dc} is DC voltage.

TABLE 1. Voltage vectors and switch states chart.

S_a	S_b	S_c	Voltage vector u
0	0	0	$u_0 = 0$
1	0	0	$u_1 = 2/3U_{dc}e^{-j\theta}$
1	1	0	$u_2 = (1/3 + j\sqrt{3}/3)U_{dc}e^{-j\theta}$
0	1	0	$u_3 = (-1/3 + j\sqrt{3}/3)U_{dc}e^{-j\theta}$
0	1	1	$u_4 = -2/3U_{dc}e^{-j\theta}$
0	0	1	$u_5 = (-1/3 - j\sqrt{3}/3)U_{dc}e^{-j\theta}$
1	0	1	$u_6 = (1/3 - j\sqrt{3}/3)U_{dc}e^{-j\theta}$
1	1	1	$u_7 = 0$

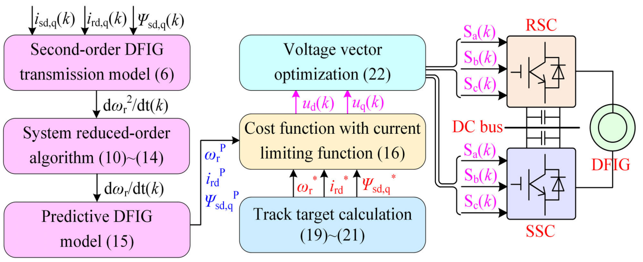

FIGURE 3. Control scheme of proposed SLMPC.

D. THE WHOLE DFIG CONTROL SCHEME

The whole system control block diagram is illustrated in Fig.3. The proposed SLMPC scheme mainly includes second-order DFIG model, system reduced-order algorithm, DFIG state variables prediction, cost function with current limitation and voltage vector optimization, which are corresponding to equation (6), (10)-(14), (15), (16) and (22), respectively. $i_{sd,q}$, $i_{rd,q}$ and $\psi_{sd,q}$ are control input variables, and S_a, S_b and S_c are control output variables for RSC and SSC.

E. TRADITIONAL CASCADED DUAL-LOOP PI-MPC STRATEGY

To make a system performance comparison, cascaded PI-MPC is referenced in [8], and designed as follows.

The outer PI controller is given as

$$i_{rd}^* = k_p(\omega_r^* - \omega_{rPI\text{-}MPC}) + k_i\int(\omega_r^* - \omega_{rPI\text{-}MPC})dt \qquad (24)$$

where k_i and k_p are integral and proportional coefficients.

The predictive equation, cost functions and optimization equation for inner MPC controller are given as

$$z = [A(k)T + 1]z(k) + BTy(k) \qquad (25)$$

$$\begin{cases} g_{SSC} &= k_{T1}|\psi_{sd}^* - \psi_{sd}^p| + k_{T2}|\psi_{sq}^* - \psi_{sq}^p| \\ g_{RSC} &= k_{T3}|i_{rd}^* - i_{rd}^p| + k_{T4}|i_{rq}^* - i_{rq}^p| \end{cases} \qquad (26)$$

$$\begin{cases} u_{opt} &= u_\gamma \\ \gamma &= \arg\min g[f_{(i,\psi)}(u_x)]\ x \in [0, 1, \ldots, 7] \end{cases} \qquad (27)$$

where k_{T1}, k_{T2}, k_{T3} and k_{T4} are weight coefficients; $z = [\psi_{sd}^p\ \psi_{sq}^p\ i_{rd}^p\ i_{rq}^p]^T$, $y = [u_{sd}\ u_{sq}\ u_{rd}\ u_{rq}]^T$,

$$A = \begin{bmatrix} -R_s/L_s & \omega_1 & \beta R_s & 0 \\ -\omega_1 & -R_s/L_s & 0 & \beta R_s \\ -\beta R_s/\alpha L_s & -\beta\omega_r/\alpha & -\lambda/\alpha & \omega_s \\ \beta\omega_r/\alpha & \beta R_s/\alpha L_s & -\omega_s & -\lambda/\alpha \end{bmatrix},$$

$$B = \begin{bmatrix} 1 & 0 & 0 & 0 \\ 0 & 1 & 0 & 0 \\ -\beta/\alpha & 0 & 1/\alpha & 0 \\ 0 & -\beta/\alpha & 0 & 1/\alpha \end{bmatrix}.$$

IV. SYSTEM SIMULATIONS

To verify proposed SLMPC strategy's efficiency and feasibility, simulated system that includes DFIG, SSC, RSC, PI-MPC controller and SLMPC controller is constructed in Fig. 4. System parameters are illustrated in Table 2, and control parameters are presented in Table 3.

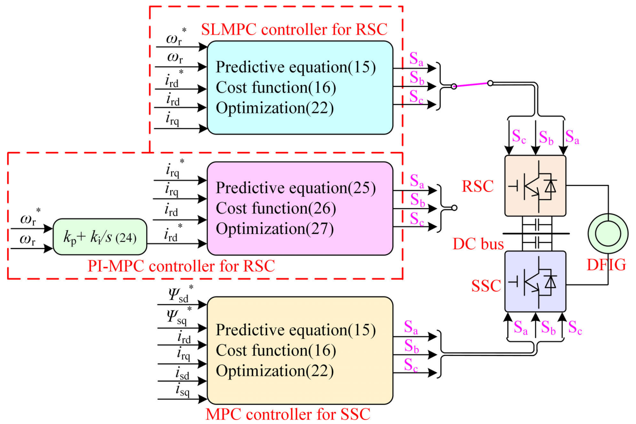

FIGURE 4. System simulation platform.

TABLE 2. System parameters.

Symbols	Quantities	Values
R_s	Stator resistance	0.88 Ω
R_r	Rotor resistance	0.88 Ω
L_r	Rotor leakage reactance	5.6 mH
L_m	Mutual inductance	87.5 mH
L_s	Stator leakage reactance	5.6 mH
n_p	Pair of poles	2
J	Moment of inertia	0.015 kg· m^2
f_s	Switching frequency	10 kHz
U_{dc}	DC voltage	650 V
V_s	Rated phase stator voltage	311 V
ω_1^*	The synchronous speed	314 rad/s

Obviously, SLMPC has less control parameters compared with PI-MPC in Fig. 4 and Table 3, which simplifies control structure and reduces parameter design difficulty. Moreover, four cases are implemented to analyse DFIG system performance under PI-MPC and SLMPC.

Case A: System steady-state performance is analysed under two control strategies at 15 and 12 m/s wind speeds.

Case B: System transient performance under two control strategies is analysed when the wind speed varies from 15 to 12 m/s.

Case C: System performance is analysed under SLMPC with dead time or not.

TABLE 3. System parameters.

Strategies	Symbols	Quantities	Values
Proposed SLMPC	k_{s1}	SSC cost function coefficient	1
	k_{s2}	SSC cost function coefficient	1
	k_{r1}	RSC cost function coefficient	1
	k_{r2}	RSC cost function coefficient	100
Traditional PI-MPC	k_p	PID proportional coefficient	1
	k_i	PID integral coefficient	5
	k_{T1}	SSC cost function coefficient	1
	k_{T2}	SSC cost function coefficient	1
	k_{T3}	RSC cost function coefficient	1
	k_{T4}	RSC cost function coefficient	1

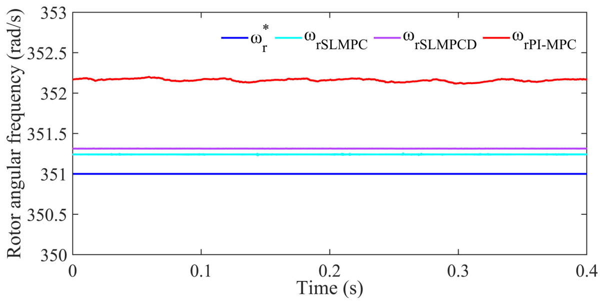

FIGURE 5. Angular frequency results under SLMPC and PI-MPC.

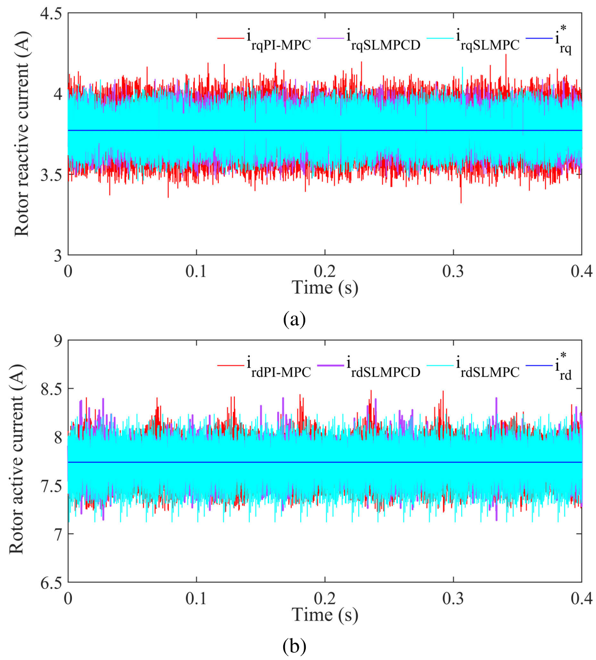

FIGURE 6. Rotor currents: a rotor reactive current; b rotor active current.

Case D: System safety performance is analysed under SLMPC with current limiting function or not.

System simulation results under two control strategies are illustrated in Figs. 5-15, where the blue curves are variables' targets. The cyan and magenta curves are system state variables with current limiting term for SLMPC and for PI-MPC respectively. And the red curves are system state variables without current limiting term for SLMPC. In addition, purple curves are system variables under SLMPC with dead time.

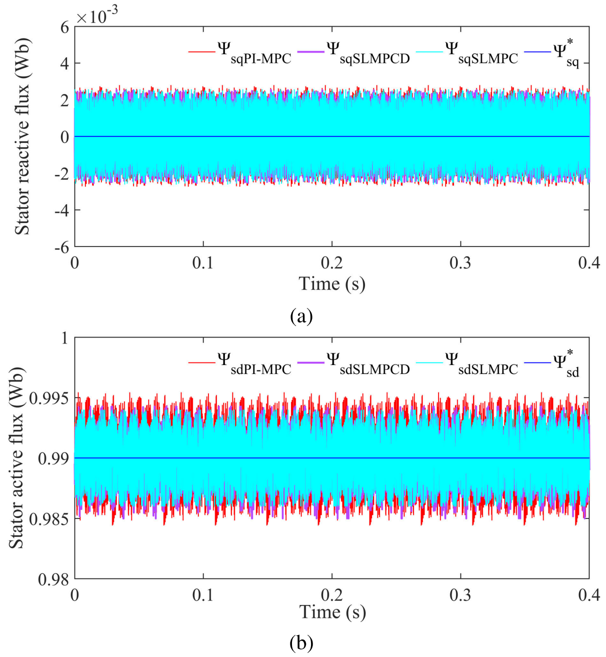

FIGURE 7. Stator fluxes: a stator reactive flux; b stator active flux.

A. SYSTEM STEADY-STATE PERFORMANCE COMPARATION

System steady-state curves are presented in Figs. 5-8 at wind speed of 15 m/s.

ω_{rSLMPC} and $\omega_{rPI\text{-}MPC}$ track stably target value of 351 rad/s, with 0.2 and 1.1 rad/s error. $i_{rqSLMPC}$ and $i_{rqPI\text{-}MPC}$ track stably target value of 3.8 A with 0.2 and 0.3 A error, and $i_{rdSLMPC}$ and $i_{rdPI\text{-}MPC}$ keep at target value of 7.77A with 0.5 and 0.6 A error. $\psi_{sqSLMPC}$ and $\psi_{sqPI\text{-}MPC}$ track target value of 0 Wb with 0.002 and 0.0025 Wb error, and $\psi_{sdSLMPC}$ and $\psi_{sdPI\text{-}MPC}$ track target value of 0.99 Wb with 0.004 and 0.005 Wb error, respectively. $i_{sqSLMPC}$ and $i_{sqPI\text{-}MPC}$ track target value of 0 A with 0.22 and 0.32 A error, and $i_{sdSLMPC}$ and $i_{sdPI\text{-}MPC}$ track target value of -7.5 A with 0.2 and 0.6 A error.

Therefore, at rated wind speed, the two strategies could make system operate stably. Besides, SLMPC has better steady-state performance with smaller steady-state error, compared with PI-MPC.

B. SYSTEM TRANSIENT PERFORMANCE COMPARATION

System transient curves are presented in Figs. 9-12 while the wind speed drops from 15 to 12 m/s at 0.5 s. In Fig. 9, 10b and 12b, ω_{rSLMPC}, $i_{rdSLMPC}$ and $i_{sdSLMPC}$ track their targets of 281 rad/s, 5 and -5 A in 0.056 s, while $\omega_{rPI\text{-}MPC}$, $i_{rdPI\text{-}MPC}$ and $i_{sdPI\text{-}MPC}$ track their targets after 0.167 s.

In Fig. 10a, 11 and 12a, i_{rq}, $\psi_{sd,q}$ and i_{sq} track stably their targets under two control strategies.

When wind speed decreases, in order to track optimal rotor speed as fast as possible, active currents (i_{sd}, i_{rd}) are transiently increased to enlarge electromagnetic torque.

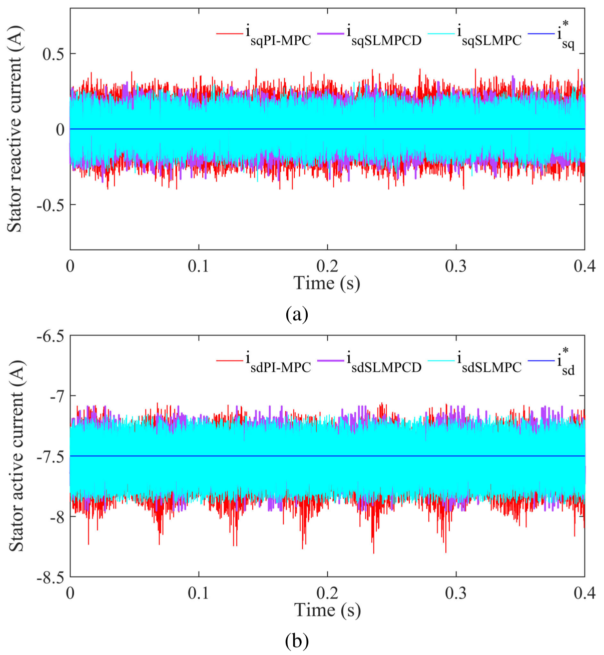

FIGURE 8. Stator currents: a stator reactive current; b stator active current.

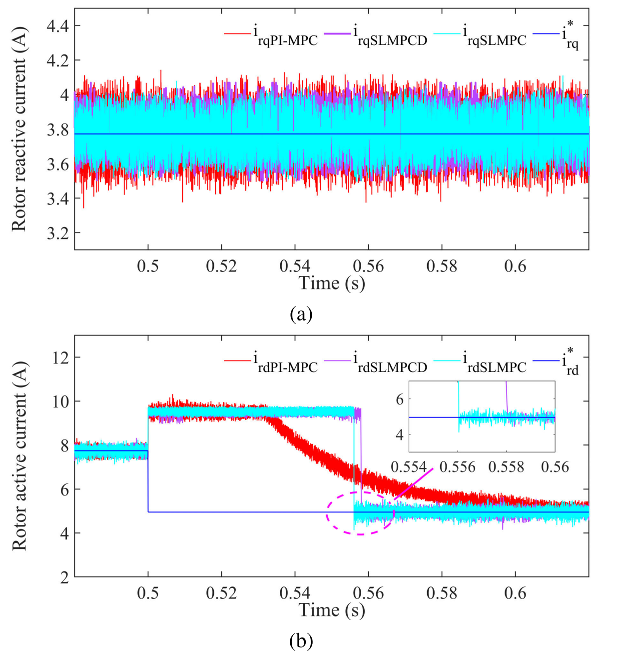

FIGURE 10. Rotor currents: a rotor reactive current; b rotor active current.

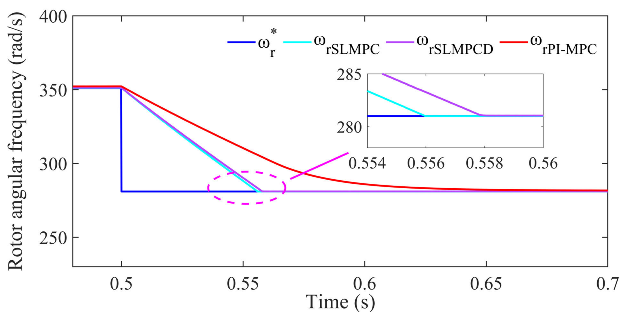

FIGURE 9. Rotor speed transient results under SLMPC and PI-MPC.

Therefore, SLMPC has better dynamic performance with 0.111 s response speed improvement to track its target compared with PI-MPC when wind speed varies.

C. SYSTEM PERFORMANCE ANALYSIS WITH DEAD TIME OR NOT

System steady-state and transient comparation results under SLMPC with dead time or not are shown in Figs.5-12 to illustrate system performance influenced by dead time of real switching device. And dead time is set about 100 ns.

In steady and transient state, system variable's curves under SLMPC with dead time are basically similar to that without dead time. Besides, SLMPC with dead time makes rotor speed error increase by 0.1 rad/s, stator reactive and active flux errors increase by 0.3 and 0.5 mWb, rotor active current error increase by 0.03 A, and system dynamic response time increase by 2 ms, compared with that without dead time. And the main reason is that control strategy has no beneficial effect on system performance during dead time. And the longer dead time is, the worse system performance is.

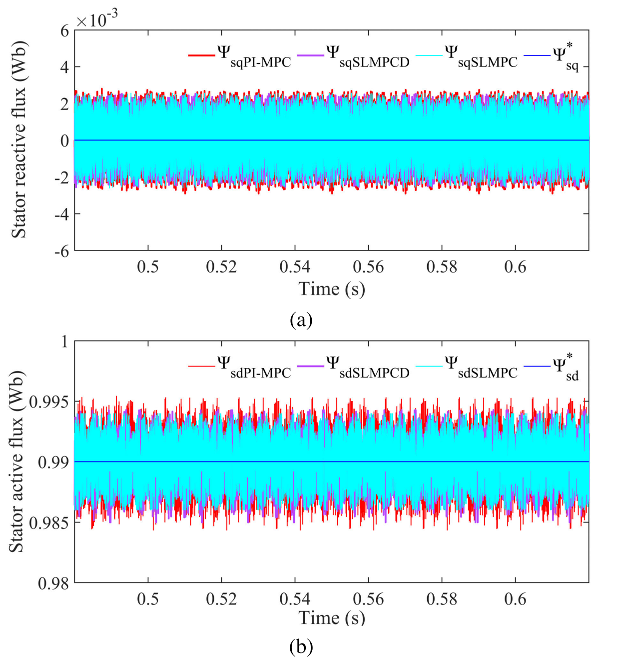

FIGURE 11. Stator fluxes: a stator reactive flux; b stator active flux.

And system performance comparation under different strategies is listed in Table 4.

D. SYSTEM SAFETY PERFORMANCE ANALYSIS WITH CURRENT LIMITING FUNCTION OR NOT

System results under SLMPC with current limiting function or not are shown in Figs. 13-15 when wind speed drops from 15 to 12 m/s at 0.5 s.

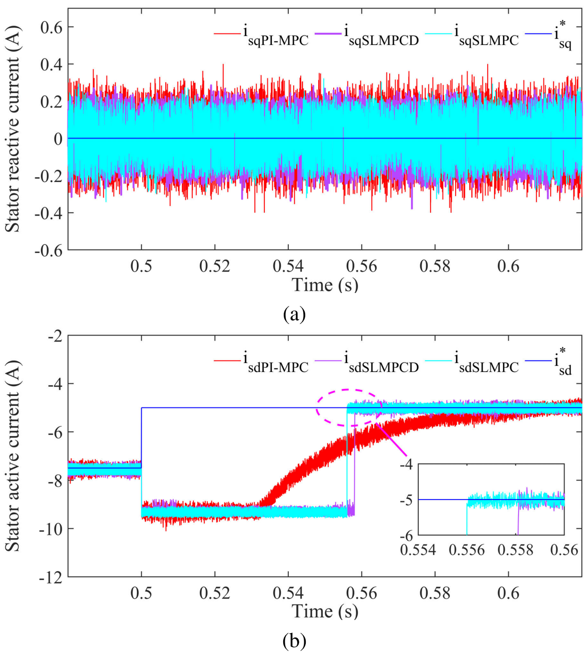

FIGURE 12. Stator currents: a stator reactive current; b stator active current.

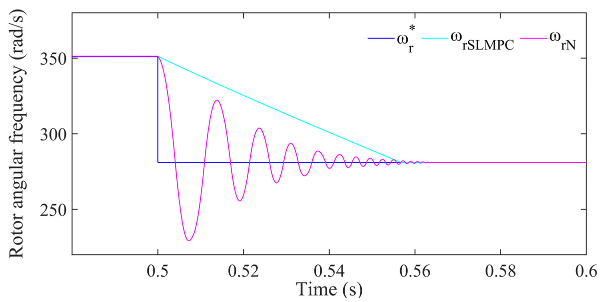

FIGURE 13. Rotor speed simulation results with current limitation.

TABLE 4. Performance comparation.

Performance	items	SLMPC	SLMPCD	PI-MPC
Steady-state error	ω_r	0.2 rad/s	0.3 rad/s	1.1 rad/s
	i_{rq}	0.2 A	0.24 A	0.3 A
	i_{rd}	0.5 A	0.53 A	0.6 A
	ψ_{sq}	2 mWb	2.3 mWb	2.5 mWb
	ψ_{sd}	4 mWb	4.5 mWb	5 mWb
	i_{sq}	0.22 A	0.25 A	0.32 A
	i_{sd}	0.2 A	0.4 A	0.6 A
Dynamic response time	ω_r	0.056 s	0.058 s	0.167 s
	i_{rd}	0.056 s	0.058 s	0.167 s
	i_{sd}	0.056 s	0.058 s	0.167 s

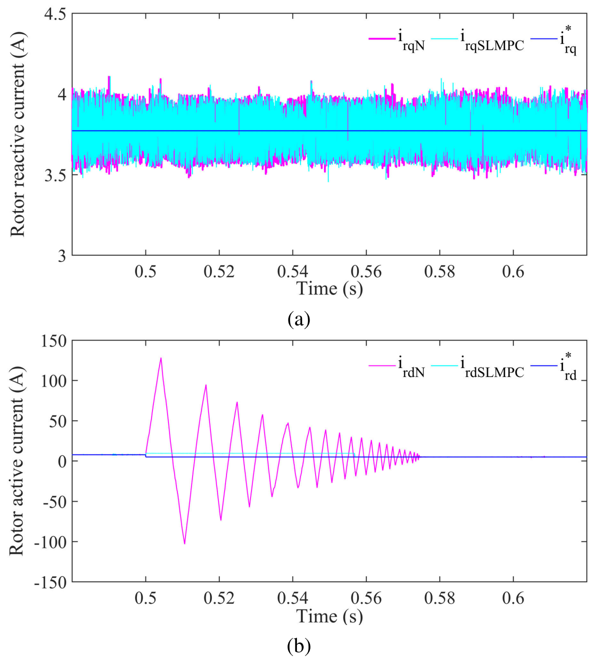

FIGURE 14. Rotor currents: a rotor reactive current; b rotor active current.

ω_{rSLMPC}, $i_{rdSLMPC}$ and $i_{sdSLMPC}$ track their targets smoothly and stably with wind speed decreasing, while ω_r, i_{rdN} and i_{sdN} fluctuate tempestuously with their max amplitudes of 47.5 rad/s, 124 A and 122.3 A. The large speed fluctuation would create huge mechanical stress and abrade gear, and excessive current might damage electrical devices.

Therefore, with current limiting function, active currents of rotor and stator could be restricted in its safety range, which guarantees system operate normally.

V. SYSTEM EXPERIMENT

To further verify the SLMPC, DFIG system experimental platform is built, which contains DFIG, RSC, SSC, emulated wind turbine and DC bus in Fig. 16, and the experimental system parameters are listed in Table 2.

A. EXPERIMENT RESULTS AT WIND SPEED OF 15 M/S

Experiment results under SLMPC are shown in Fig. 17.

The magenta curve (ω_{rSLMPC}) keeps stably at 351 rad/s; The orange and blue curves (u_{sSLMPC}, i_{sSLMPC}) are sinusoid curves with the same frequency (50 Hz) and phase, and their amplitudes are 311 V and 6.5 A; The green curve (i_{rSLMPC}) is sinusoid with amplitude of 7.5 A and frequency of 6 Hz.

Therefore, system state variables (ω_r, u_s, i_s, i_r) operate stably with ideal values at wind speed of 15 m/s.

B. EXPERIMENT RESULTS DURING WIND SPEED VARIATION

Experiment curves under two control strategies are illustrated in Fig. 18 while the wind speed reduces from 15 to 12 m/s.

The orange curve (ω_{rSLMPC}) decreases from 351 to 281 rad/s in 0.06 s; amplitudes of the blue and magenta curves (i_{sSLMPC}, i_{rSLMPC}) decrease from 6.5 to 4 A and from 7.5 to 5.5 A in 0.06 s respectively, in Fig. 18a. However, the orange, dark-cyan and magenta curves ($\omega_{rPI\text{-}MPC}$, $i_{rPI\text{-}MPC}$ and $i_{sPI\text{-}MPC}$) track their targets after 0.17 s, in Fig. 18b.

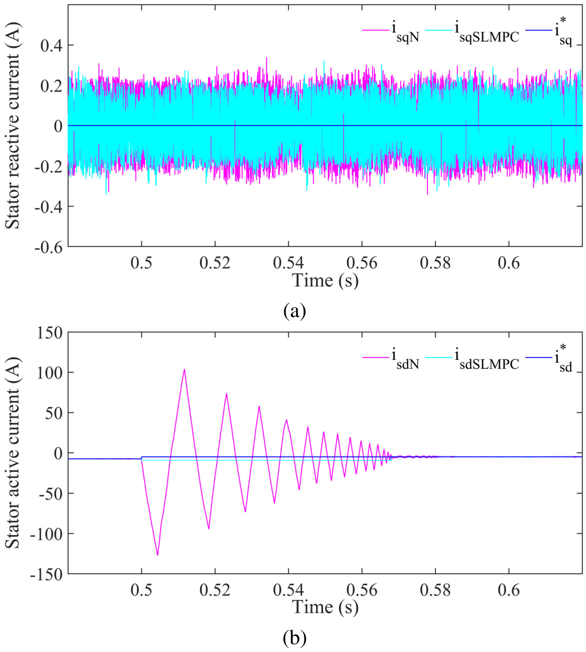

FIGURE 15. Stator currents: a stator reactive current; b stator active current.

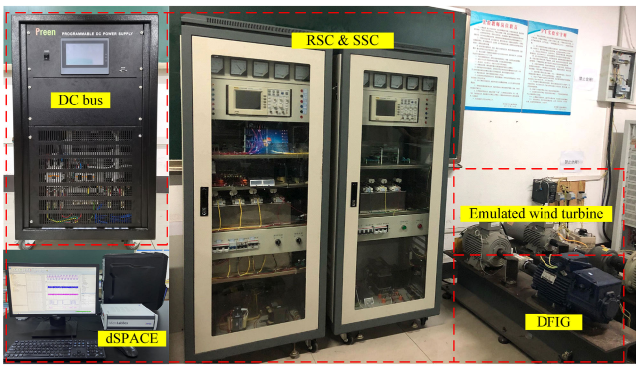

FIGURE 16. System experimental platform.

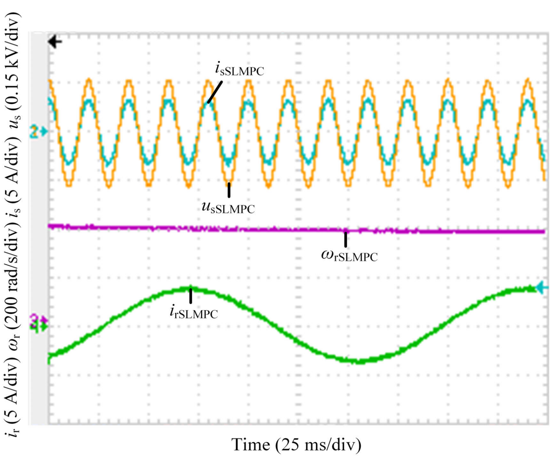

FIGURE 17. The variations of ω_r, u_s, i_s, i_r (SLMPC).

Therefore, proposed SLMPC has excellent transient and steady-state performance compared with traditional cascaded PI-MPC.

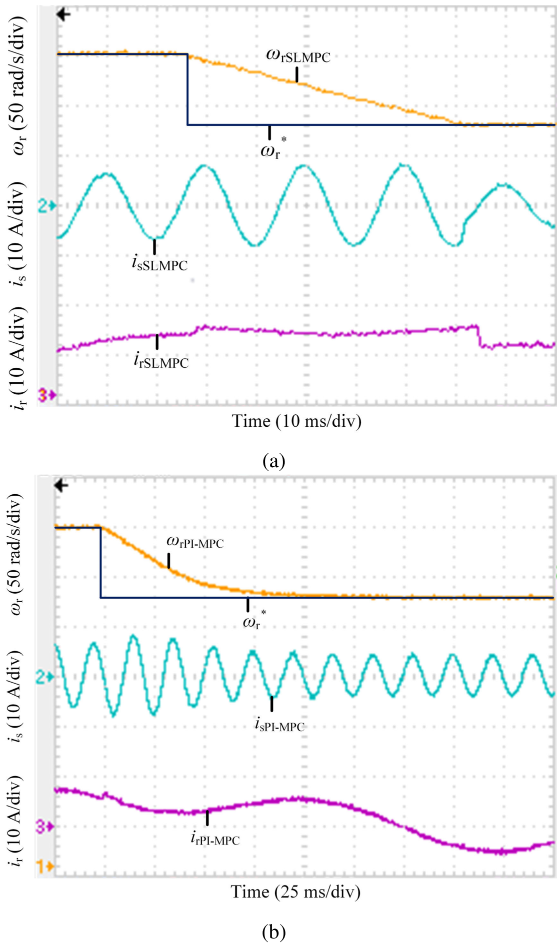

FIGURE 18. The variations of ω_r, i_s, i_r: a SLMPC b PI-MPC.

VI. CONCLUSION

In the paper, a SLMPC strategy for DC-based DFIG is proposed to simplify system control structure and enhance system dynamic response capacity. Based on simulated and experimental results, we might come to following conclusions.

1. The proposed SLMPC omits the intermediate link and reduces control parameters' amounts from 6 to 4, which decreases system dynamic response time by 0.111 s, and lowers rotor speed error by 0.3 rad/s, stator reactive and active flux errors by 0.5 and 1 mWb, and rotor active current error by 0.1 A, compared with traditional PI-MPC.

2. System reduced-order discretization algorithm is adopted to convert the complicated prediction model to simple first-order model, which effectively tackles the problems of dT_m/dt acquisition and $d^2\omega_r/dt^2$ trace and simplifies MPC design complexity.

3. The cost function with current limiting function is adopted to limit current in safety range to effectively protect system from overcurrent, which is verified on the simulation.

REFERENCES

[1] A. M. S. Yunus, A. Abu-Siada, M. A. S. Masoum, M. F. El-Naggar, and J. X. Jin, "Enhancement of DFIG LVRT capability during extreme short-wind gust events using SMES technology," *IEEE Access*, vol. 8, pp. 47264–47271, 2020, doi: 10.1109/ACCESS.2020.2978909.

[2] Z. Rafiee, R. Heydari, M. Rafiee, M. R. Aghamohammadi, and F. Blaabjerg, "Enhancement of the LVRT capability for DFIG-based wind farms based on short-circuit capacity," *IEEE Syst. J.*, vol. 16, no. 2, pp. 3237–3248, Jun. 2022.

[3] R. Yang, J. Jin, Q. Zhou, M. Zhang, S. Jiang, and X. Chen, "Superconducting magnetic energy storage integrated current-source DC/DC converter for voltage stabilization and power regulation in DFIG-based DC power systems," *J. Mod. Power Syst. Clean Energy*, pp. 1–14, 2022, doi: 10.35833/MPCE.2022.000051.

[4] B. Hamid, I. Hussain, S. J. Iqbal, B. Singh, S. Das, and N. Kumar, "Optimal MPPT and BES control for grid-tied DFIG-based wind energy conversion system," *IEEE Trans. Ind. Appl.*, vol. 58, no. 6, pp. 7966–7977, Nov. 2022.

[5] G. D. Marques and M. F. Iacchetti, "DFIG topologies for DC networks: A review on control and design features," *IEEE Trans. Power Electron.*, vol. 34, no. 2, pp. 1299–1316, Feb. 2019.

[6] R. Yang, J. Jin, Q. Zhou, S. Mu, and A. Abu-Siada, "Superconducting magnetic energy storage based DC unified power quality conditioner with advanced dual control for DC-DFIG," *J. Mod. Power Syst. Clean Energy*, vol. 10, no. 5, pp. 1385–1400, Sep. 2022.

[7] J. Liu, W. Yao, J. Wen, J. Fang, L. Jiang, H. He, and S. Cheng, "Impact of power grid strength and PLL parameters on stability of grid-connected DFIG wind farm," *IEEE Trans. Sustain. Energy*, vol. 11, no. 1, pp. 545–557, Jan. 2020.

[8] S. Yan, A. Zhang, H. Zhang, J. Wang, and B. Cai, "Optimized and coordinated model predictive control scheme for DFIGs with DC-based converter system," *J. Mod. Power Syst. Clean Energy*, vol. 5, no. 4, pp. 620–630, Jul. 2017.

[9] H. Shao, X. Cai, Z. Li, D. Zhou, S. Sun, L. Guo, Y. Cao, and F. Rao, "Stability enhancement and direct speed control of DFIG inertia emulation control strategy," *IEEE Access*, vol. 7, pp. 120089–120105, 2019, doi: 10.1109/ACCESS.2019.2937180.

[10] Y. Zhang, C. Klabunde, and M. Wolter, "Frequency-coupled impedance modeling and resonance analysis of DFIG-based offshore wind farm with HVDC connection," *IEEE Access*, vol. 8, pp. 147880–147894, 2020, doi: 10.1109/ACCESS.2020.3015614.

[11] Z. Din, J. Zhang, Y. Zhu, Z. Xu, and A. El-Naggar, "Impact of grid impedance on LVRT performance of DFIG system with rotor crowbar technology," *IEEE Access*, vol. 7, pp. 127999–128008, 2019, doi: 10.1109/ACCESS.2019.2938207.

[12] Y. Wang, J. Su, J. Lai, B. Xie, Y. Shi, and H. Yu, "Equivalent and identification of integrated coupling parameter of variable speed constant frequency brushless doubly fed generator," *J. Power Electron.*, vol. 22, no. 1, pp. 61–71, Jan. 2022.

[13] C. Wu and H. Nian, "Improved direct resonant control for suppressing torque ripple and reducing harmonic current losses of DFIG-DC system," *IEEE Trans. Power Electron.*, vol. 34, no. 9, pp. 8739–8748, Sep. 2019.

[14] Z. Dong, Z. Li, L. Du, Y. Liu, and Z. Ding, "Coordination strategy of large-scale DFIG-based wind farm for voltage support with high converter capacity utilization," *IEEE Trans. Sustain. Energy*, vol. 12, no. 2, pp. 1416–1425, Apr. 2021.

[15] Y. Xiao, B. Fahimi, M. A. Rotea, and Y. Li, "Multiple reference frame-based torque ripple reduction in DFIG-DC system," *IEEE Trans. Power Electron.*, vol. 35, no. 5, pp. 4971–4983, May 2020.

[16] Y. Song, X. Wang, and F. Blaabjerg, "High-frequency resonance damping of DFIG-based wind power system under weak network," *IEEE Trans. Power Electron.*, vol. 32, no. 3, pp. 1927–1940, Mar. 2017.

[17] F. N. Mazgar, M. T. Hagh, and S. Tohidi, "ESS equipped DFIG wind farm with coordinated power control under grid fault conditions," *J. Power Electron.*, vol. 21, no. 1, pp. 173–183, Jan. 2021.

[18] H. Nian, C. Cheng, and Y. Song, "Coordinated control of DFIG system based on repetitive control strategy under generalized harmonic grid voltages," *J. Power Electron.*, vol. 17, no. 3, pp. 733–743, May 2017.

[19] M. Parvez, M. F. M. Elias, N. A. Rahim, F. Blaabjerg, D. Abbott, and S. F. Al-Sarawi, "Comparative study of discrete PI and PR controls for single-phase UPS inverter," *IEEE Access*, vol. 8, pp. 45584–45595, 2020, doi: 10.1109/ACCESS.2020.2964603.

[20] Y.-W. Geng, H.-W. Liu, R.-X. Deng, F.-F. Tian, H.-F. Bai, and K. Wang, "Research on a multi-objective control strategy for current-source PWM rectifiers under unbalanced and harmonic grid voltage conditions," *J. Power Electron.*, vol. 18, no. 1, pp. 171–184, Jan. 2018.

[21] M. S. R. Saeed, W. Song, L. Huang, and B. Yu, "Double-vector-based finite control set model predictive control for five-phase PMSMs with high tracking accuracy and DC-link voltage utilization," *IEEE Trans. Power Electron.*, vol. 37, no. 12, pp. 15234–15244, Dec. 2022.

[22] M. S. Mousavi, S. A. Davari, V. Nekoukar, C. Garcia, and J. Rodriguez, "A robust torque and flux prediction model by a modified disturbance rejection method for finite-set model-predictive control of induction motor," *IEEE Trans. Power Electron.*, vol. 36, no. 8, pp. 9322–9333, Aug. 2021.

[23] A. Olloqui, J. L. Elizondo, M. Rivera, M. E. Macías, O. M. Micheloud, R. Peña, and P. Wheeler, "Model-based predictive rotor current control strategy for indirect power control of a DFIM driven by an indirect matrix converter," *IEEE Trans. Energy Convers.*, vol. 36, no. 2, pp. 1510–1516, Jun. 2021.

[24] H. A. G. Al-Kaf and K. Lee, "Low complexity MPC-DSVPWM for current control of PMSM using neural network approach," *IEEE Access*, vol. 10, pp. 132596–132607, 2022, doi: 10.1109/ACCESS.2022.3230356.

[25] S. Odhano, S. Rubino, M. Tang, P. Zanchetta, and R. Bojoi, "Stator current-sensorless-modulated model predictive direct power control of a DFIM with magnetizing characteristic identification," *IEEE J. Emerg. Sel. Topics Power Electron.*, vol. 9, no. 3, pp. 2797–2806, Jun. 2021.

[26] S. Yan, C. Li, Y. Cui, X. Gao, and Y. Cai, "An improved FCS-MPC based on virtual vector expansion and sector optimization for 2L-VSCs," *IEEE Access*, vol. 10, pp. 127450–127460, 2022, doi: 10.1109/ACCESS.2022.3227211.

[27] M. Aguirre, S. Kouro, C. A. Rojas, and S. Vazquez, "Enhanced switching frequency control in FCS-MPC for power converters," *IEEE Trans. Ind. Electron.*, vol. 68, no. 3, pp. 2470–2479, Mar. 2021.

[28] Y. Wang, F. Liu, S. Chen, G. Shen, and Q. Wang, "Prediction errors analysis and correction on FCS-MPC for the cascaded H-bridge multilevel inverter," *IEEE Trans. Ind. Electron.*, vol. 69, no. 8, pp. 8264–8273, Aug. 2022.

[29] I. Jlassi and A. J. M. Cardoso, "Enhanced and computationally efficient model predictive flux and power control of PMSG drives for wind turbine applications," *IEEE Trans. Ind. Electron.*, vol. 68, no. 8, pp. 6574–6583, Aug. 2021.

[30] A. Dekka, B. Wu, V. Yaramasu, R. L. Fuentes, and N. R. Zargari, "Model predictive control of high-power modular multilevel converters—An overview," *IEEE J. Emerg. Sel. Topics Power Electron.*, vol. 7, no. 1, pp. 168–183, Mar. 2019.

[31] L. Yan, M. Dou, H. Zhang, and Z. Hua, "Speed-sensorless dual reference frame predictive torque control for induction machines," *IEEE Trans. Power Electron.*, vol. 34, no. 12, pp. 12285–12295, Dec. 2019.

[32] Y. Zhang, J. Jiao, D. Xu, D. Jiang, Z. Wang, and C. Tong, "Model predictive direct power control of doubly fed induction generators under balanced and unbalanced network conditions," *IEEE Trans. Ind. Appl.*, vol. 56, no. 1, pp. 771–786, Jan. 2020.

[33] M. Darabian and A. Jalilvand, "Predictive control strategy to improve stability of DFIG-based wind generation connected to a large-scale power system," *Int. Trans. Electr. Energy Syst.*, vol. 27, no. 5, p. e2300, May 2017, doi: 10.1002/etep.2300.

[34] M. E. Zarei, C. V. Nicolás, and J. R. Arribas, "Improved predictive direct power control of doubly fed induction generator during unbalanced grid voltage based on four vectors," *IEEE J. Emerg. Sel. Topics Power Electron.*, vol. 5, no. 2, pp. 695–707, Jun. 2017.

[35] R. V. Jacomini and A. J. S. Filho, "Finite control set applied to the direct power control of a DFIG operating under voltage sags," *IEEE Trans. Sustain. Energy*, vol. 10, no. 2, pp. 952–960, Apr. 2019.

[36] G. F. Gontijo, T. C. Tricarico, B. W. França, L. F. da Silva, E. L. van Emmerik, and M. Aredes, "Robust model predictive rotor current control of a DFIG connected to a distorted and unbalanced grid driven by a direct matrix converter," *IEEE Trans. Sustain. Energy*, vol. 10, no. 3, pp. 1380–1392, Jul. 2019.

[37] P. Kou, D. Liang, J. Li, L. Gao, and Q. Ze, "Finite-control-set model predictive control for DFIG wind turbines," *IEEE Trans. Autom. Sci. Eng.*, vol. 15, no. 3, pp. 1004–1013, Jul. 2018.

SHAOMIN YAN received the B.S. degree in mechanical and electrical engineering from the Qilu University of Technology, in 2001, the M.S. degree in electrical and electronic engineering from the Zhejiang University of Technology, in 2004, and the Ph.D. degree in electrical engineering from Xi'an Jiaotong University, in 2017. He is currently an Associate Professor with the School of Engineering, Qufu Normal University, Rizhao, China. His current research interests include wind energy conversion systems and power electronics.

XIAOJIE GAO received the B.S. degree in electrical engineering from Qufu Normal University, in 2020, where he is currently pursuing the M.S. degree with the School of Engineering. His current research interests include power electronics and HVDC transmission.

YONGHAO LU received the B.S. and M.S. degrees in electrical engineering from Qufu Normal University, in 2018 and 2021, respectively. His current research interests include power electronics and DFIG control.

YUE CUI received the B.S. degree in electrical engineering from Qufu Normal University, in 2020, where he is currently pursuing the M.S. degree with the School of Engineering. His current research interests include power electronics and intelligent control.

YUHAN CAI received the B.S. degree in electrical engineering from Qufu Normal University, in 2020, where she is currently pursuing the M.S. degree with the School of Engineering. Her current research interests include power electronics and PMSG control.